RSC Advances

ROYAL SOCIETY OF CHEMISTRY

www.rsc.org/advances

RSC Advances

ARTICLE

Understanding the formation mechanism and the 3D structure of $Mo(S_xSe_{1-x})_2$ nanoflowers

Received 00th January 20xx,
Accepted 00th January 20xx

DOI: 10.1039/x0xx00000x

www.rsc.org/

Meiron O. E.[a], Houben, L.[b], Bar-Sadan M.[a]

Nanoflowers of layered materials are promising building blocks for photocatalysis due to their unique morphology and exposed edges. Colloidal synthesis of MoS_2, $MoSe_2$ and their alloys was used to produce fine nanoflowers with tunable composition. The alloys follow Vegard's law, showing homogeneous composition. They exhibit fully tunable optical properties, where the exciton positions change with alloy composition. Samples annealed under vacuum retain their fine morphology and their composition, which closely follows the feed ratio. Time series analysis was used to investigate the formation mechanism. The results support a growth mechanism of fast-precipitating amorphous material, followed by crystallization of a few layers of small sheets, which curl and tangle around themselves. Electron tomography of the time series reveals a perforated structure without a dense core, supporting the suggested growth mechanism. These structures show multiple exposed edge sites, making them promising materials for applications such as photocatalysis.

Introduction

Transition metal dichalcogenides (TMDs) have been widely researched in the past decade due to their tunable band structure, optical properties and electronic characteristics[1]. Because of these properties, they were suggested for a wide array of applications such as electrodes for Li ion batteries[2,3], gas sensors[4], electrodes for hydrogen evolution reaction (HER)[5,6] and thin film transistors[7]. Thinning the materials into their ultimate dimension of a single layer has a significant effect on their physical and chemical properties[8]. Specifically, the transition from indirect to direct bandgap has a large impact on the versatility and functionality of several TMDs such as MoS_2 and $MoSe_2$. One method of tuning the material's properties is through morphology control. Numerous methods have been shown to increase the number of exposed edges in TMDs, and specifically in MoS_2[9,10], since it was realized that the active sites for catalysis are the flakes' edges[6].

One of the most promising morphologies for catalysis is nanoflowers[11], which exhibit a relatively large ratio between exposed edges and basal planes. These materials are usually produced via a hydrothermal synthesis in an autoclave[12]. Electrodes synthesized using the above-mentioned technique were successfully used to reduce polysulfides in quantum dot sensitized solar cells[11]. Although these materials are very promising, closer inspection reveals that the petaled edges are more than 10 nm thick. Having more than 15 layers prevents the utilization of quantum size effects for improving the activity of the exposed layer edges[13]. In addition, hydrothermal synthesis requires high pressure in order to produce supercritical water, which makes it only suitable for small scale production. By switching to colloidal synthesis, a larger number of parameters can be controlled, ultimately leading to better morphology control. Recently, $MoSe_2$ nanoflowers were synthesized via colloidal synthesis by using $MoO_2(acac)_2$ and dibenzyldiselenide[14]. The resulting ultrathin structures resembled the petaled particles. However, they were an order of magnitude smaller, and had only 2-5 layers at the edges. Their exact growth mechanism is still unclear. These fine petaled structures were selenium-deficient, and demonstrated better efficiency for hydrogen evolution.

Morphology control is not the only approach to modifying TMD properties. Doping and alloying arise as promising methods for chemically modifying TMD properties. First principles studies have shown that atom dopants can induce changes in physical properties such as conductivity and magnetism in TMDs[15,16]. Among other qualities, the semiconducting nature of TMDs was switched from *p*- to *n*-type and vice versa using different dopants[16–19]. Alloys are also used in order to tune the electronic structure of TMDs, specifically the materials' bandgap and band alignment. The two most researched alloys are $Mo_xW_{1-x}S_2$[20] and $Mo(S_xSe_{1-x})_2$ [21–23]. Both are produced primarily using solid state chemistry techniques such as chemical vapor deposition (CVD) and chemical vapor transport (CVT). Early density function theory research predicted that $Mo(S_xSe_{1-x})_2$ should be stable at room temperature[24], making it one of the most researched alloys of MoS_2. Recent work explored the catalytic activity of $Mo(S_xSe_{1-x})_2$ alloys grown by CVT[25]. The alloys are more effective cathode materials than either pure MoS_2 or $MoSe_2$ towards HER[14].

[a] Ben-Gurion University of the Negev, Department of Chemistry, Beer Sheva .
[b] Chemical Research Support, Weizmann Institute of Science, Rehovot, Israel

Electronic Supplementary Information (ESI) available: movies of the electron tomography tilt series, a scroll through the tomogram slices and a rotation of the 3D visualization is available in the ESI. See DOI: 10.1039/x0xx00000x

Even though alloying and doping play a crucial role in fine tuning the electronic properties of TMDs, only a handful of papers have been published so far on these materials. The biggest challenge is to reproducibly produce alloys with a specific composition in large quantities. Using CVD or CVT, only partial control is achieved over the alloys' compositions. A previous study showed that by varying the substrate position inside the CVD furnace relative to the precursors, the alloy composition can be controlled[22]. However, it causes a composition gradient on the substrate, making it impractical for large scale applications. In order to resolve these issues, a different chemical approach has to be explored.

A recent report describes the colloidal synthesis of $Mo(S_xSe_{1-x})_2$ in an oleylamine and octylamine solution, using $MoCl_5$ and elemental S and Se[26]. The alloyed nanoflakes show improved performance of hydrogen production compared to pure MoS_2 and $MoSe_2$. However, one major problem that occurs when preparing HER electrodes is the loss of the exposed edges due to aggregation of the layers. In flower-like particles, more active edges are exposed, which will possibly lead to better performance.

In this work, we synthesized alloys of $Mo(S_xSe_{1-x})_2$ nanoflowers using a colloidal process. Control over the composition of the alloys was achieved using a bottom-up strategy at relatively low temperatures (≤300°C). Chalcogenide precursors with similar reactivities were used in order to form the desired homogenous alloy for each Se/S composition. The produced alloys exhibited tunable band gaps as a function of composition. The mechanism of formation was evaluated through a time series experiment and electron tomography of the particles, revealing that the particles formed from an amorphous material, and that there was no dense core at the center of the particles. This finding confirms a previously suggested formation mechanism, where separated sheets fold onto each other to form the nanoflower structures.

Methods

Dibenzyldiselenide (DBSe) and its sulfur analog, dibenzyldisulfide (DBS), were used in order to produce the alloys. Our main assumption was that performing the reaction above the decomposition temperature of both the sulfur and selenium precursors will lead to the homogeneous incorporation of the chalcogenides in the synthesized alloys, and that their ratio will be dictated by their relative concentrations in solution.

Synthesis

All of the reactions were performed using standard Shlenk line technique. All of the chemicals were of analytical grade, and were used as received without further purification. Dibenzyldiselenide (DBSe) 95% (Alfa Aesar), dibenzyldisulfide (DBS) 98% (Alfa Aesar), bis(acetylacetonate) dioxomolybenum(VI) 95% (Strem chemicals inc.), oleylamine (OA) 70% (Aldrich), toluene ACS grade (Gadot), ethanol ACS grade (Romicol), 1-butanol ACS grade (Alfa Aesar). Distilled water (DW) was used, unless specified otherwise.

The desired molar ratios of $MoO_2(acac)_2$ and chalcogenide precursors were degassed in a three-necked flask with 10 ml OA under vacuum at 110 °C for 15-30 min. The flask was backfilled with N_2, and heated to 300 °C for 20 min. After the flask was cooled to room temperature, the product was precipitated by adding excess n-butanol. The crude product was collected by centrifugation. The product was washed with the following solutions: 50:50 (toluene:ethanol), 70:30 (toluene:ethanol), pure toluene, twice with 70:30 (ethanol:DW), and once with acetone. It was then dried overnight under vacuum. The materials produced using this method were amorphous. In order to improve their crystallinity, the products were sealed in a quartz ampule under vacuum and annealed at 873 °C in a tube furnace for 16-24 h.

Microscopy

TEM images were obtained on a 120 kV FEI T-12 or a 120 kV Jeol T1230. High-resolution transmission electron microscopy (HR-TEM) images were acquired on a 200 kV Jeol 2100F. Dilute solutions of materials, dispersed in organic or aqueous solvents, were dropped on either lacy carbon or ultrathin amorphous carbon on 400 mesh copper grids, and were allowed to air-dry. For HR-TEM analysis, the grids were dried in an ultra-high vacuum (UHV) oven at 30-40 °C for at least 24 h.

Characterization

UV-Vis spectra were collected on a Shimadzu UV-3600. Annealed samples were dispersed in isopropanol (Isop) using a bath sonicator for at least 5 min. The obtained spectra were normalized to exciton B intensity. Powder XRD data were collected using a Panalytical Empyrean powder diffractometer equipped with a position-sensitive X'Celerator detector using Cu K_α radiation (λ=1.5405 Å) operated at 40 kV and 30 mA. Raman spectra were collected on a Jobin-Yvon LabRam HR 800 micro-Raman system equipped with a Synapse CCD detector. The excitation source was an Argon laser (514.5 nm) with a power of 0.05 mW on the sample. The laser was focused with an x100 objective to a spot of about 2 µm. All the measurements were performed using a D2 filter. Inductive coupled plasma mass spectrometer (ICP-MS) spectra were collected on an Agilent 7700 series ICP-MS. For the ICP-MS, the samples were dissolved in ACS grade 10% H_2O_2 for 24 hours. The reaction was stopped by adding 10 µl of 99.999% pure 70% HNO_3 and diluted with 18.2 MΩ·cm water.

Electron tomography

Tilt series of high-resolution TEM phase-contrast images were acquired on a FEI F20 TWIN electron microscope. The tilt increment was 3° in a range of ±70°. Tomograms were reconstructed using the iterative simultaneous reconstruction technique, after cross-correlation alignment and iterative feedback displacement refinement[27]. MeVisLab[28] was used for the visualization of tomogram data.

Results and discussion

In contrast to chemical vapor techniques, where S and Se vapors have almost the same reactivity, the reactivity of the precursors is an important parameter in colloidal syntheses. In order to ensure that both the S and Se precursors decompose and incorporate into the crystal structure, the reaction temperature was set above the precursors' decomposition temperature, which is ~170 °C for DBS in organic solutions[29] and under 240 °C for DBSe[14]. The syntheses yielded nanoflowers with similar morphology and size (100-200 nm) for all the compositions of 0, 20, 50, 80, and 100% S in the feed ratio (See Figure 1, left panels). The needle-like moieties in the center of the nanoflower are small sheets viewed edge-on. The rest of the flower structure is delicate and thin, with one to a few layers of TMD viewed in projection.

HR-TEM images revealed that the edges were constructed of 3-5 layers, and that the number of layers is retained after annealing, as can be seen in Figure 2. In agreement with the literature, the crystallinity of TMDs produced at a low temperature is poor. These materials are often described as amorphous MoS_x or MoS_3 [30,31]. Therefore, the syntheses products were annealed at above the growth temperature of MoS_2 (873 °C). During the annealing process, the materials are sensitive to oxidation[32], so they require an inert atmosphere (N_2) or a reducing environment (such as a mixture of 5% H_2 in Ar). Alternatively, the annealing can be performed under vacuum conditions in a sealed quartz ampule, preventing the loss of the more volatile S during the annealing stage. Annealing the samples under vacuum in a sealed quartz ampule retains the size and morphology of the delicate flowers without thickness or stoichiometry change, as can be seen in Figures 1-2 and Table 1. The annealed samples were used for further characterization.

In order to determine the alloys' compositions more accurately, ICP-MS spectrometry was used. Table 1 summarizes the results of the different alloys. Measuring the concentration of S using ICP-MS introduces substantial errors: it has many known interferences, it is only about 15% ionized in the Ar plasma, and all isotopes are subject to severe overlapping from mainly O- and N-based signals. Therefore, only the Mo:Se ratio was calculated, and S content was determined based on the Se ratios. We used the synthesis of pure $MoSe_2$ to deter-

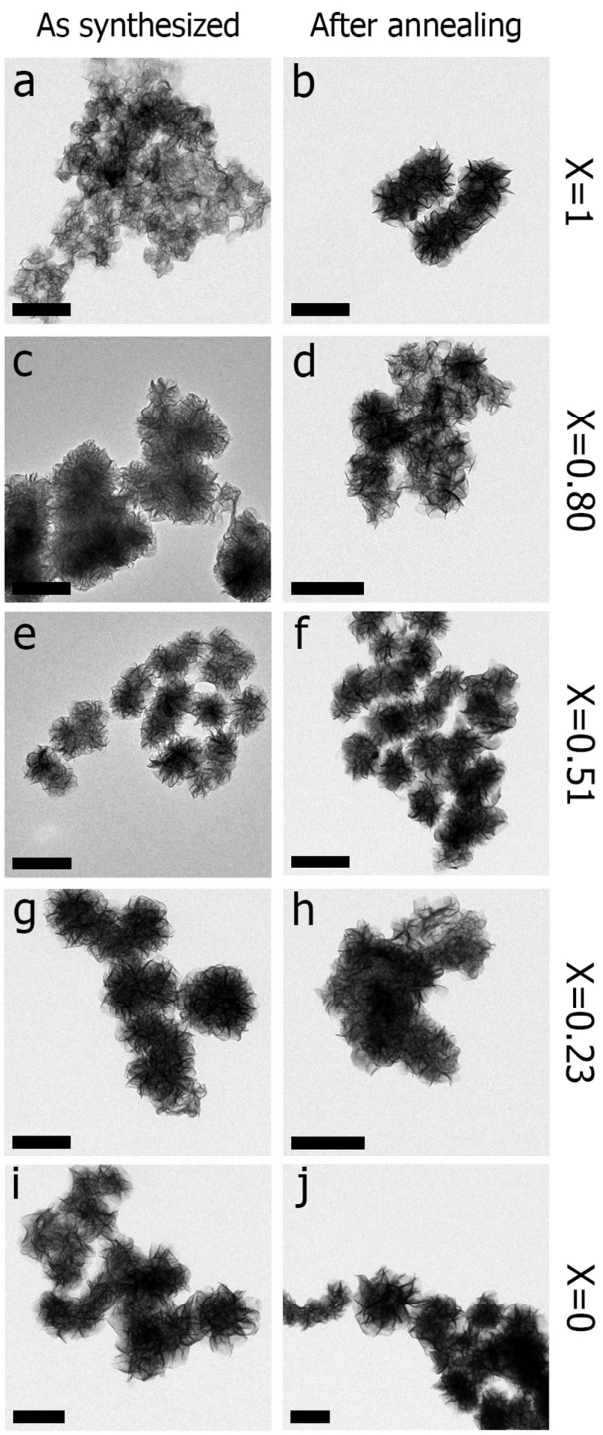

Figure 1. TEM images of $Mo(S_xSe_{1-x})_2$ alloys. The left panel shows the as-synthesized materials. The right panel shows the products after annealing in vacuum. The scale bar in all the images is 200 nm.

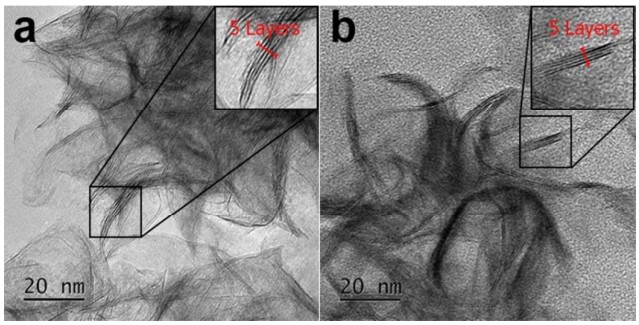

Figure 2. HRTEM images of $Mo(S_{0.51}Se_{0.49})_2$ alloy. (a) As-synthesized particle showing 3-5 layers at the edges. (b) After annealing in vacuum, showing that no structural changes occurred during the annealing stage. Insets show enlarged areas of the 5-layered edges.

Table 1. S:Se ratio calculated from ICP-MS results

Feed ratio		Experimental value	
S	**Se**	S	Se
0.0	**1.0**	0.00	1.00±0.03
0.2	**0.8**	0.23	0.77±0.03
0.5	**0.5**	0.51	0.49±0.03
0.8	**0.2**	0.80	0.20±0.03
1.0	**0.0**	1.00	0.00±0.03

mine the Mo:Se ratio of 1:1.62, in accordance with previously reported Mo-rich $MoSe_{2-x}$ nanoflowers[14]. The results for the ternary compounds were normalized to the $MoSe_2$ values, and showed a very good fit of the measured S:Se with the feed ratio.

Pure MoS_2 and $MoSe_2$ have hexagonal structures of the $P_{63}/_{mmc}$ space group (PDF-37-1492 for MoS_2 and 77-1715 for $MoSe_2$). Figure 3a shows XRD data of pure and alloyed materials. There is a shift towards higher diffraction angles with increasing S content, in accordance with a reduction in cell parameters as

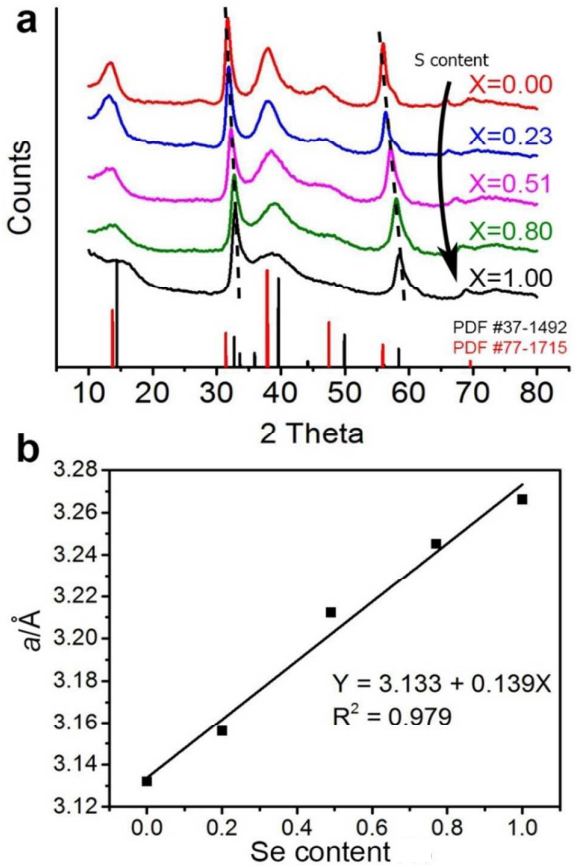

Figure 3. (a) XRD patterns of $Mo(S_xSe_{1-x})_2$ alloys. Dashed lines are added as guides. Black and red vertical lines are the PDF spectra of MoS_2 and $MoSe_2$, respectively. (b) *a* cell parameter vs. Se fraction.

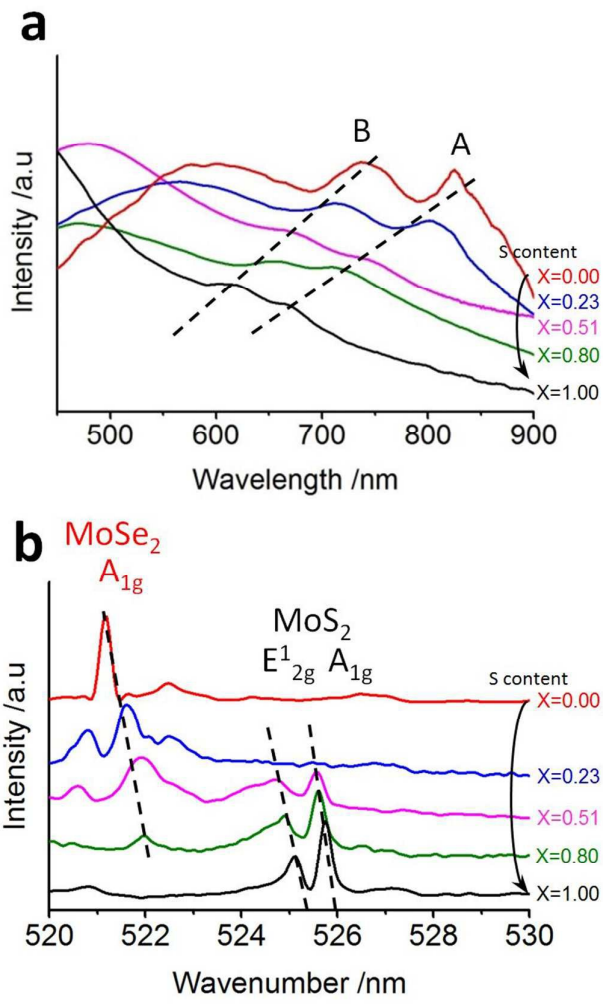

Figure 4. (a) Absorption spectra of $Mo(S_xSe_{1-x})_2$ alloys showing the shift in excitons A and B positions from MoS_2 (black line) to $MoSe_2$ (red line). (b) Raman spectra of $Mo(S_xSe_{1-x})_2$ alloys showing the increase in the E^1_{2g} and A_{1g} modes of MoS_2 and the decrease of the A_{1g} $MoSe_2$ mode with increasing S content. Dashed lines are added as guides

the larger Se atoms are replaced by smaller S atoms. Dashed lines were added to assist in tracking the transition. Cell parameters of the different alloys were calculated, and the *a* lattice parameter was plotted against the Se content (Figure 3b). The plot has good linear correlation, which is consistent with Vegard's law. It suggests that S and Se are homogenously distributed in the lattice. The UV-Vis spectra of the pure and alloyed materials contain the two excitons of MoS_2 and $MoSe_2$, as can be seen in Figure 4a. Both excitons shift gradually to the lower wavelengths as the S content increases, further confirming the ternary mixture's homogeneity. In accordance, the Raman spectra presented in Figure 4b show a gradual increase in the MoS_2 E^1_{2g} and A_{1g} modes with increasing S content, as previously reported[22]. As the Se content fraction decreases, there is a dampening and decrease in the $MoSe_2$ and A_{1g} mod-

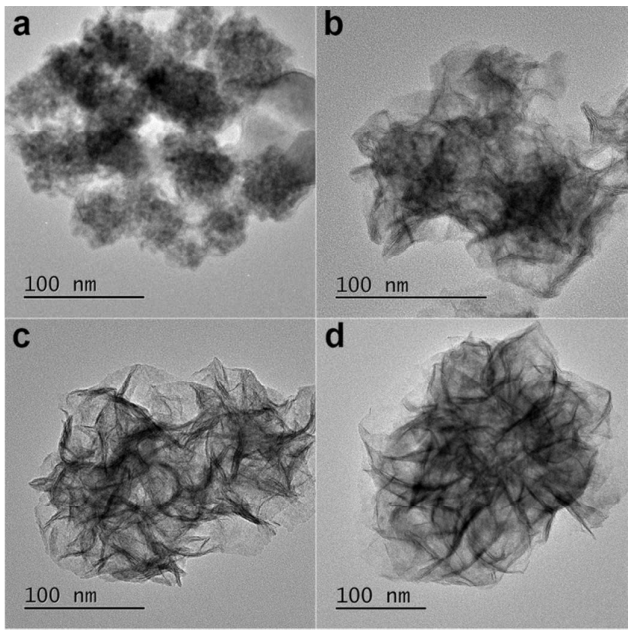

Figure 5. Time series analysis of $MoSe_2$ particles. TEM images of $MoSe_2$ nanoflowers taken at times: (a) 1 min. (b) 3 min. (c) 5 min. (d) 10 min.

es.

In order to investigate the sensitivity of the alloyed nanoflowers to alternative synthetic protocols, different precursors were used for the synthesis. We found that replacing $MoO_2(acac)_2$ with different Mo precursors, e.g. $MoCl_5$, MoO_3, $Na_2MoO_4 \cdot 2H_2O$ or $(NH4)_2MoO_4$, prevents the formation of the nanoflower structures and produces other morphologies (See figure S1 in the ESI). Changing the S or Se precursor to elemental S and Se also resulted in loss of the flower-like morphology. The combination of $MoO_2(acac)_2$ and DBSe/DBS proved to be unique in achieving the nanoflowers in oleylamine.

Previous reports provide two growth schemes: either the initial structures are amorphous sheets that curl around themselves to produce flowers[14], or the flower-like structure is the nucleus of the growth, followed by an outward growth of the thin petals[33]. These two mechanisms have different reaction rates: a faster reaction yields the sheets morphology, and a slower reaction produces the flower morphology, which is then extended by growth.

To better understand the formation mechanism, we performed a time series analysis. The synthesis procedure was slightly modified as follows: the molybdenum and selenium precursors were degassed in two separate flasks. The molybdenum solution was heated to 300 °C, and the selenium solution was then injected rapidly to start the reaction. Aliquots of 1 ml were quenched in 1-butanol at four different time points during the reaction, and analyzed. Figure 5a-d presents TEM images of the aliquots at times 1, 3, 5 and 10 min, respectively. In addition, electron tomography was used to understand the 3D structure of the particles from the time series and to determine the growth mechanism. Using electron tomography, it is possible to isolate a slice of the analyzed volume without the superimposed information from the top and bottom parts of the sample. Figure 6 presents the 2D images from the time series at times 1, 3 and 5 minutes, alongside the corresponding slices from the 3D reconstructions.

Figure 5a and 6a show that after 1 minute, small ~50 nm amorphous clusters form in the solution, that later serve as a reservoir of material for the crystallization stages. After 3 minutes, the amorphous material is consumed to form curled and tangled sheets that crystallize within the amorphous clusters. Voids are also created in this process, since the crystallized form is denser than the amorphous cluster. Adjacent clusters also merge, as shown in figure 5b and 6b. There is no preferred growth direction of the sheets, and they appear to favor random lateral growth. It is important to note that no dense core is visualized, ruling out a radial growth mechanism where a crystalized seed serves as the substrate for further growth. The amount of amorphous material decreases with time, with a slight increase in the number of crystalline layers (from 1-3 after 3 minutes to 3-5 after 5 minutes). The major change seen in the particles over time is the crystallization of the amorphous material, with a relatively minor change in lateral size after 5 minutes. We therefore conclude that the growth relies on the reservoir of material produced by the initial cluster formation. Our findings support the formation m-

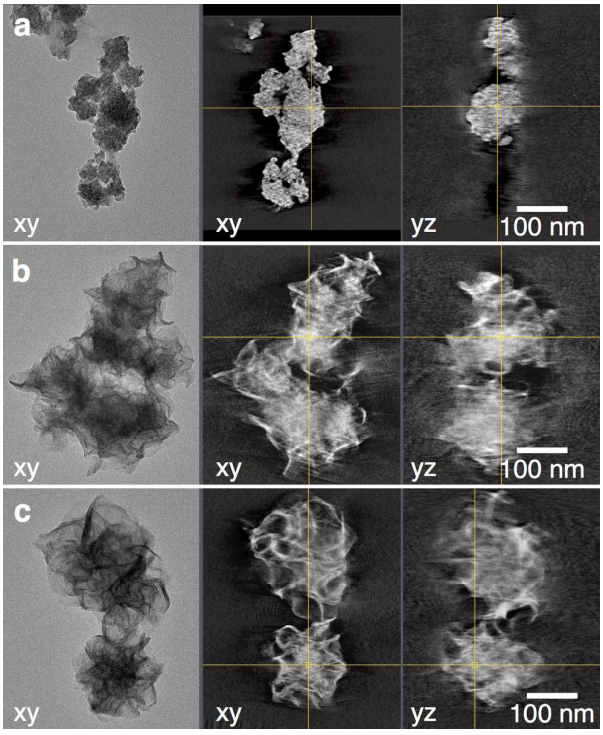

Figure 6. Tomogram data for the time series analysis of $MoSe_2$ particles. TEM images and tomogram slices of $MoSe_2$ nanoflowers taken at times: (a) 1 min. (b) 3 min. (c) 5 min. Each panel displays a zero tilt TEM image in the xy-projection plane on the left, and two central tomogram slices in the xy- and yz-plane on the right.

echanism described in Ref. 14 and in contrast to the one described in ref. 33.

A consequence of this reaction mechanism is the control of the homogeneity of the final product, since the efficient formation of an amorphous material reservoir allows the incorporation of both S and Se during crystallization to form homogenous solid solutions, without relying on their reactivity and diffusion in the solution. In order to confirm that the same mechanism governs the growth of the ternary compounds, tomography of the $Mo(S_{0.51}Se_{0.49})_2$ sample was performed. Figure 7 presents three slices of the tomogram from a central section of the particle. The slices in Figure 7b-d show three cut planes in different directions from the tomogram. They show that there are voids at the core of the particle, in accordance with the growth mechanism described above. The particle seems perforated, with delicate petals extruding from the center, like in the pure material's structure. An additional 3D visualization is shown in Figure 7a, featuring the sponge-like structure which lacks a dense center. Additional movies of the tilt series, a scroll through the tomogram slices and a rotation of the 3D visualization is available in the ESI.

Conclusions

In summary, we present the synthesis of $Mo(S_xSe_{1-x})_2$ alloys using a facile colloidal synthesis that produces flower-like particles with a large number of exposed edges. The nanoflowers were Mo-rich, their chalcogen compositions closely followed the feed ratio, and they were maintained after annealing in vacuum. The properties confirm a homogenous mixture of the chalcogens. The nanostructures lack a dense core that could serve as a nucleation seed. They grow from initial amorphous clusters that individually crystallize into small curled sheets and aggregate to larger particles. The formation of the amorphous clusters, which later serve as material reservoirs for the crystallization, facilitates the efficient mixing of reactants and the production of homogenous ternary materials. These structures have many exposed edges, making them promising candidates for applications such as photocatalysis.

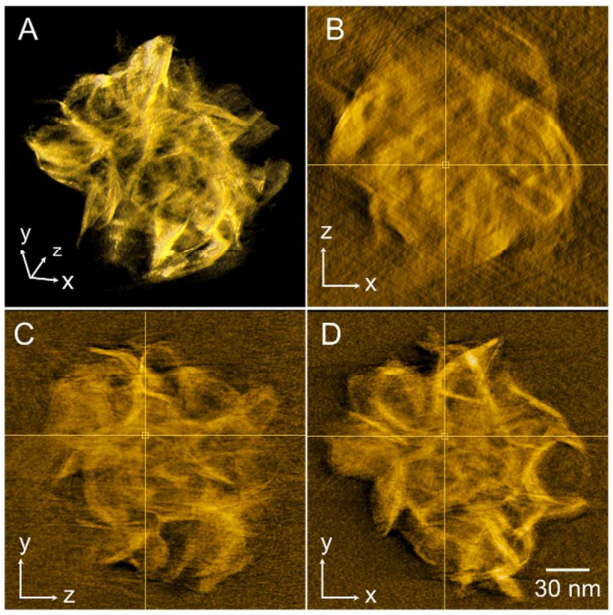

Figure 7. Electron tomography of a single $Mo(S_{0.51}Se_{0.49})_2$ nanoflower. (A) Volume visualization (voxel projection). (B-D) Slices from the tomogram showing cut planes through the center of the nanoflower.

Acknowledgements

We thank Lena Yadgarov and Ilit Cohen Ofri for their kind help with the ICP-MS analysis, and Pradipta Sankar Maiti, Sagi Appel and Lana Binyamin for their consult and support. This work was supported by the Focal Technology Area (FTA) project on "Inorganic nanotubes (INT) from nanomechanics to improved nanocomposites" and by the Israeli Centers of Research Excellence (I-CORE) program (Center No. 152/11) and ISF grant 475/12.

Notes and references

1 Wang, Q. H., Kalantar-Zadeh, K., Kis, A., Coleman, J. N. & Strano, M. S. Electronics and Optoelectronics of Two-Dimensional Transition Metal Dichalcogenides. *Nature Nanotech.* 2012, **7,** 699–712.

2 Nandi, D. K., Sen, U. K., Choudhury, D., Mitra, S. & Sarkar, S. K. Atomic Layer Deposited MoS_2 as a Carbon and Binder Free Anode in Li-ion Battery. *Electrochim. Acta* 2014, **146,** 706–13.

3 Guo, J., Chen, X., Yi, Y., Li, W. & Liang, C. Layer-Controlled Synthesis of Graphene-Like MoS_2 From Single Source Organometallic Precursor for Li-ion Batteries. *RSC Adv.* 2014, **4,** 16716–20.

4 Li, H., Wu, J., Yin, Z. & Zhang, H. Preparation and Applications of Mechanically Exfoliated Single-Layer and Multilayer MoS_2 and WSe_2 Nanosheets. *Acc. Chem. Res.* 2014, **47,** 1067–75.

5 Kibsgaard, J., Chen, Z., Reinecke, B. N. & Jaramillo, T. F. Engineering the Surface Structure of MoS_2 to Preferentially Expose Active Edge Sites for Electrocatalysis. *Nature Mater.* 2012, **11,** 963–9.

6 Jaramillo, T. F. *et al.* Identification of Active Edge Sites for Eectrochemical H_2 Evolution From MoS_2 Nanocatalysts. *Science* 2007, **317,** 100–2.

7 Kwak, J. Y. *et al.* Electrical Characteristics of Multilayer MoS_2 FET's with MoS_2/Graphene Heterojunction Contacts. *Nano Lett.* 2014, **14,** 4511–6.

8 Splendiani, A. *et al.* Emerging Photoluminescence In Monolayer MoS_2. *Nano Lett.* 2010, **10,** 1271–5.

9 Shi, Y., Li, H. & Li, L.-J. Recent Advances In Controlled Synthesis of Two-Dimensional Transition Metal Dichalcogenides Via Vapour Deposition Techniques. *Chem. Soc. Rev.* 2014, **44,** 2744–56.

10 Yan, Y., Xia, B., Xu, Z. & Wang, X. Recent Development of Molybdenum Sulfides as Advanced Electrocatalysts for Hydrogen Evolution Reaction. *ACS Catalysis* 2014, **4,** 1693–705.

11 Finn, S. T. & Macdonald, J. E. Petaled Molybdenum Disulfide Surfaces: Facile Synthesis of a Superior Cathode for QDSSCs. *Adv. Energy Mater.* 2014, **4,** 1400495.

12 Huang, W., Xu, Z., Liu, R., Ye, X. & Zheng, Y. Tungstenic Acid Induced Assembly of Hierarchical Flower-Like MoS_2 spheres. *Mater. Res. Bull.* 2008, **43,** 2799–805.

13 Sheng, B., Liu, J., Li. Z., Wang, M., Zhu, K., Qiu, J., Wang, J., Effects of Excess Sulfur Source on the Formation and Photocatalytic Properties of Flower-Like MoS_2 Spheres by Hydrothermal Synthesis. *Mater. Lett.* 2015, **144**, 153-6.
14 Zhou, X. *et al.* Fast Colloidal Synthesis of Scalable Mo-Rich Hierarchical Ultrathin $MoSe_{2-x}$ Nanosheets for High-Performance Hydrogen Evolution. *Nanoscale* 2014, **6,** 11046–51.
15 Yue, Q., Chang, S., Qin, S. & Li, J. Functionalization of Monolayer MoS_2 by Substitutional Doping: A First-Principles Study. *Phys. Lett. A* 2013, **377,** 1362–7.
16 Tian, X. *et al.* Effects of 3d Transition-Metal Doping on Electronic and Magnetic Properties of MoS_2 Nanoribbons. *Phys. Chem. Chem. Phys.* 2014, **17,** 1831–6.
17 Fang, H. *et al.* Degenerate n-doping of Few-Layer Transition Metal Dichalcogenides by Potassium. *Nano Lett.* 2013, **13,** 1991–5.
18 Laskar, M. R. *et al.* p-Type Doping of MoS_2 Thin Films Using Nb. *Appl. Phys. Lett.* 2014, **104,** 092104.
19 Lin, Y.-C. *et al.* Doping Properties and Phase Transition in Single-Layer MoS_2. *Microsc. Microanal.* 2014, **20,** 1750–1.
20 Dumcenco, D. O., Chen, K. Y., Wang, Y. P., Huang, Y. S. & Tiong, K. K. Raman Ttudy of 2H-$Mo_{1-x}W_xS_2$ Layered Mixed Crystals. *J. Alloys Compd.* 2010, **506,** 940–3.
21 Wang, H. *et al.* Multifunctional TiO_2 Nanowires-Modified Nanoparticles Bilayer Film for 3D Dye-Sensitized Solar Cells. *Optoelectron. Adv. Mater. Rapid Commun.* 2010, **4,** 1166–1169.
22 Li, H., Duan, X., Wu, X. & Zhuang, X. Growth of Alloy $MoS_{2x}Se_{2(1-x)}$ Nanosheets With Fully Tunable Chemical Compositions and Optical Properties. *J. Am. Chem. Soc.* 2014, **136,** 3756–9.
23 Gong, Y. *et al.* Band Gap Engineering and Layer-by-Layer Mapping of Selenium-Doped Molybdenum Disulfide. *Nano Lett.* 2014, **14,** 442–9.
24 Komsa, H.-P. & Krasheninnikov, A. V. Two-Dimensional Transition Metal Dichalcogenide Alloys: Stability and Electronic Properties. *J. Phys. Chem. Lett.* 2012, **3,** 3652–6.
25 Kiran, V., Mukherjee, D., Jenjeti, R. N. & Sampath, S. Active Guests in the MoS_2/$MoSe_2$ Host Lattice: Efficient Hydrogen Evolution Using Few-Layer Alloys of $MoS_{2(1-X)}Se_2X$. *Nanoscale* 2014, **6,** 12856–6.
26 Gong, Q. *et al.* Ultrathin $MoS_{2(1-x)}Se_{2x}$ Alloy Nanoflakes For Electrocatalytic Hydrogen Evolution. *ACS Catal.* 2015, **5,** 2213–9.
27 Houben, L. & Bar Sadan, M. Refinement Procedure for the Image Alignment in High-Resolution Electron Tomography. *Ultramicroscopy* 2011, **111,** 1512–152.
28 Ritter, B. F. *et al.* Medical Image Analysis: A Visual Approach. *IEEE Pulse* 2011, **2,** 60–70.
29 Plaza, S. & Mazurkiewicz, B. Thermal Decomposition Mechanism of Dibenzyl Disulphide and Its Load-Carrying. *Wear* 1994, **174,** 209–16.
30 Ahmad, M. *et al.* Charge Conduction and Relaxation in MoS_2 Nanoflakes Synthesized by Simple Solid State Reaction. *J. Appl. Phys.* 2013, **114,** 043710.
31 Yan, Y. *et al.* Ultrathin MoS_2 Nanoplates With Rich Active Sites As Highly Efficient Catalyst for Hydrogen Evolution. *ACS Appl. Mater. Interfaces* 2013, **5,** 12794–8.
32 Schuffenhauer, C., Wildermuth, G., Felsche, J. & Tenne, R. How Stable are Inorganic Fullerene-Like Particles? Thermal Analysis (STA) of Inorganic Fullerene-Like NbS_2, MoS_2, and WS_2 In Oxidizing and Inert Atmospheres In Comparison With the Bulk Material. *Phys. Chem. Chem. Phys.* 2004, **6,** 3991–4002.
33 Sun, D., Feng, S., Terrones, M. & Schaak, R. E. Formation and Interlayer Decoupling of Colloidal $MoSe_2$ Nanoflowers. *Chem. Mater.* 2015, **27,** 3167–75.